ChemComm
Chemical Communications

Accepted Manuscript

This article can be cited before page numbers have been issued, to do this please use: Y. Yu, X. Song, Y. Li, P. Wang, L. Cheng, Y. Yang, G. He and L. Cao, *Chem. Commun.*, 2025, DOI: 10.1039/D5CC03589A.

ROYAL SOCIETY OF CHEMISTRY

rsc.li/chemcomm

ChemComm

View Article Online
DOI: 10.1039/D5CC03589A

COMMUNICATION

Angle-controlled synthesis and redox property of tetraphenylethene-based hexacationic triangular macrocycle

Received 00th January 20xx,
Accepted 00th January 20xx

DOI: 10.1039/x0xx00000x

Yang Yu,[a,‡] Xiaowen Song,[a,‡] Yawen Li,[b,‡] Pingxia Wang,[a] Lin Cheng,[a] Ying Yang,[a,*] Gang He,[b,*] and Liping Cao[a,*]

A tetraphenylethene-based hexacationic triangular macrocycle ($T^{6+}\cdot 6PF_6^-$) was synthesized via the Zincke reaction using angle-controlled synthesis strategy. Under the chemical or electrochemical reduction conditions, $T^{6+}\cdot 6PF_6^-$ can undergo two-step reversible and stable redox transformations, accompanied by a distinct visual color change.

The rapid advancement of macrocyclic chemistry has played a pivotal role in the progress of supramolecular chemistry and materials, significantly driving their practical applications.[1-5] As a result, the design and synthesis of novel macrocycles with unique geometries and exceptional properties have become a major research frontier.[6-8] By precisely controlling the size, geometry, and stoichiometry of precursor building blocks, a variety of macrocyclic compounds with predetermined dimensions and shapes can be synthesized. For example, by exploiting the directionality and predictability of metal-ligand coordination interactions, a range of supramolecular coordination complexes (SCCs) can be assembled through coordination-driven self-assembly.[9-10] Various linking ligands, in combination with metal acceptors with angles of 60°, 90°, 120°, or 180°, have been employed to construct rhomboids, triangles, squares, hexagons, and other polygonal shapes.[11-15] In the field of covalent synthesis of macrocycles, a series of shape-persistent macrocyclic structures have also been synthesized with specific three-dimensional shapes by manipulating the angles of reactive sites, such as molecular cages, etc.[16-19]

The varying sizes and angles of precursor building blocks have inspired the design and synthesis of a wide range of macrocycles. One of the most successful examples is the cyclobis(paraquat-p-phenylene) cyclophane, known as the "blue box," first reported by Stoddart et al. [20] However, a significant limitation of this method is its inability to synthesize macrocycles with directly connected aromatic units, as S_N2 reactions do not occur between pyridine and aromatic halides. To overcome this challenge, the Zincke reaction offers a potential solution for synthesizing pyridinium-containing macrocycles, where the cationic nitrogen is functionalized with aryl groups.[21-22] Several examples of macrocycles synthesized using this approach have already been reported.[23] The viologen fragment formed in the Zincke reaction exhibits favourable redox properties, undergoing two reversible single-electron reductions. These reductions can be triggered either by chemical reagents or external stimuli such as applied voltage or light. As a result, viologen derivatives have found broad applications in electrochromic and photochromic devices.[24-28]

Angle-controllable synthesis approach is a general and high-yielding synthetic strategy that requires the complementary molecular modules to have a robust structure with predefined bite angles[29] and appropriate stoichiometric ratios,[30-32] in order to effectively obtain a wide variety of 2D and 3D macrocycles with predefined shapes and symmetry.[33] Herein, we report a tetraphenylethene(TPE)-based hexacationic triangular macrocycle using the aforementioned strategy, which is prepared by reacting 180° linear Zincke salt compound and aromatic amines with 60° angle in 1:1 stoichiometric ratio (Scheme 1). Two TPE-based aromatic amines precursors (**S1** and **S2**) were utilized to perform as angle-controlling building blocks,[24-25] linear bipyridinium derivative (**S3**) was chosen as linker.[23] Further reactions between TPE precursors and **S3** lead to synthesis of hexacationic triangular macrocycle ($\mathbf{T}^{6+}\cdot 6PF_6^-$) and dumbbell-shaped reference ($\mathbf{D}^{2+}\cdot 2PF_6^-$)[24]. Non-luminous $\mathbf{T}^{6+}\cdot 6PF_6^-$ exhibited bright reddish-brown color by addition of various poor solvents, indicating its aggregation-Induced emission (AIE) property. Moreover, $\mathbf{T}^{6+}\cdot 6PF_6^-$ and $\mathbf{D}^{2+}\cdot 2PF_6^-$ possess favorable redox properties. The first and second reduction potentials of viologen fragments from $\mathbf{D}^{2+}$ to $\mathbf{T}^{6+}$ exhibit increasingly negative values, while their LUMO energy levels gradually rise, indicating a gradual weakening of electron-accepting ability and unfavorable conditions for corresponding reduction reactions. The transformation from $\mathbf{T}^{6+}$ to the radical $\mathbf{T}^{3(+\bullet)}$ and subsequently to the neutral **T** can be achieved under redox conditions.

The synthesis of the cationic macrocycle $\mathbf{T}^{6+}\cdot 6PF_6^-$ typically complied with these following procedures. The diamino-TPE precursor **S2** was selected, which exhibits structural robustness with predefined ~60° angles. As a result, **S2** and **S3** could be controlled for synthesis of macrocycle $\mathbf{T}^{6+}\cdot 6PF_6^-$ via one-pot Zincke reaction under the appropriate stoichiometric ratio (1:1). $\mathbf{T}^{6+}\cdot 6PF_6^-$ was fully characterized by ^1H and ^{13}C NMR spectroscopy and electrospray ionization time-of-flight mass spectrometry (ESI-TOF-MS) (Figures S1-S3). Compound $\mathbf{D}^{2+}$ were synthesized from monoamino-TPE precursor **S1** and **S3**, according to the published procedures.[34]

Single crystals of $\mathbf{T}^{6+}\cdot 6PF_6^-$ were obtained by slow vapor diffusion of isopropyl ether into an acetonitrile solution of $\mathbf{T}^{6+}\cdot 6PF_6^-$ at room temperature. The crystal structure (Figure 1a) revealed that three 4,4′-bipyridine-1,1′-diium units and three TPE units formed a triangular cavity (17.317 Å) within an individual molecule of $\mathbf{T}^{6+}$.

[a]*College of Chemistry and Materials Science, Northwest University, Xi'an 710069, P. R. China. E-mail: yingyang@nwu.edu.cn, chcaoliping@nwu.edu.cn.*
[b]*Frontier Institute of Science and Technology, Xi'an Jiaotong University, Xi'an, Shaanxi, 710054 P. R. China. E-mail: ganghe@mail.xjtu.edu.cn.*
† Electronic supplementary information (ESI) available: see DOI: 10.1039/x0xx00000x.
‡ These authors contributed equally to this work.

Given the right-handed (*P*-) and left-handed (*M*-) rotation of TPE units, two conformational isomers, *PPM*-$\mathbf{T}^{6+}$ and *MMP*-$\mathbf{T}^{6+}$, were identified in the lattice of $\mathbf{T}^{6+}$. The difference in the rotational conformation of the TPE units between *PPM*-$\mathbf{T}^{6+}$ and *MMP*-$\mathbf{T}^{6+}$ resulted in the formation of a mesomeric state for the whole system. In the unit cell, both wave-like and serrated stacking structures were formed by multiple C-H…π interactions (d = 2.83-2.84 Å) between TPE units (Figures 1b-c). Interestingly, these C-H···π interactions induced the alignment and parallel arrangement of $\mathbf{T}^{6+}$ molecules into 1D nanotube-like assembles. Adjacent 1D double nanotubes, oriented at opposite angles, then formed 2D nanotube layers in a zigzag alternating pattern (Figure 1d). Ultimately, these 2D nanotube layers stacked in parallel, revealing a 3D nanotubular framework (Figure S4).

Photophysical experiments showed that $\mathbf{T}^{6+}\cdot 6PF_6^-$ exhibits different trends in absorption and emission intensity under the regulation of solvent effect. The UV-vis spectra of $\mathbf{T}^{6+}\cdot 6PF_6^-$ revealed two maximum absorption peaks corresponding to bipyridine and TPE in different solvents including acetone, 1,4-Dioxane, DMF, EA, MeOH, H_2O, MeCN, THF, $CHCl_3$, CH_2Cl_2, and DMSO (Figures S5). The results on luminescence characteristics indicated that $\mathbf{T}^{6+}\cdot 6PF_6^-$ did not exhibit significant luminescence behaviour in good solvent system. Under different solvent systems, the emission of $\mathbf{T}^{6+}\cdot 6PF_6^-$ exhibited a bright reddish-brown color, precisely centered at 555nm, while maintaining consistent and stable optical properties (Figures S6). Among them, adding 90% CH_2Cl_2 (poor solvent) to the MeCN (good solvent) solution of $\mathbf{T}^{6+}\cdot 6PF_6^-$ could significantly enhance fluorescence (Figure S7), indicating that $\mathbf{T}^{6+}\cdot 6PF_6^-$ with TPE components displayed aggregation-Induced emission (AIE) property.

To investigate the redox characteristics of $\mathbf{T}^{6+}$, the electrochemical properties were examined via cyclic voltammetry (CV) and differential pulse voltammetry (DPV). Compared to the reduction peaks of the reported dumbbell-shaped $\mathbf{D}^{2+}$ (-0.55 and -0.90 V) (Figures S8–S9), $\mathbf{T}^{6+}$ exhibited two reversible reduction peaks (-0.56 and -0.93 V), suggesting that $\mathbf{T}^{6+}$ can accept six electrons in a 2e$^-$ sequence, resulting in three distinct redox states. These findings indicate that $\mathbf{T}^{6+}$ has favourable redox properties. Furthermore, from the electrochemical data, the LUMO energy level of $\mathbf{T}^{6+}$ was calculated to be -4.24 eV (Figure S14, Table S1). In comparison, the LUMO energy level of $\mathbf{D}^{2+}$ is -4.25 eV. Notably, the first and second reduction potentials of the viologen fragments in $\mathbf{T}^{6+}$ are increasingly negative relative to $\mathbf{D}^{2+}$, while their LUMO energy levels gradually increase, reflecting a weakening of the electron-accepting ability and less favourable conditions for reduction reactions.

The local electrostatic potential values for $\mathbf{T}^{6+}/\mathbf{D}^{2+}$ were mapped on the isosurfaces of their electron density. As we expect, the two reversible single-electron reductions of $\mathbf{T}^{6+}$ were achieved through chemical reduction (Figure 2a), which was proved by observation of a decrease in electrostatic potential near the viologen units, indicating that these units are the primary sites for reduction (Figures 2b-2c). Radical $\mathbf{T}^{3(+\bullet)}$ was gradually generated by adding zinc powder to a DMF solution of $\mathbf{T}^{6+}$ under a nitrogen atmosphere, accompanied by a transition in the solution color to dark green. Two characteristic absorption peaks of the radical, at 660 nm and 720 nm, were observed in the UV-visible spectrum (Figure 2d). The radical nature of $\mathbf{T}^{3(+\bullet)}$ was further confirmed by electron paramagnetic resonance (EPR) spectroscopy (Figure 2e).

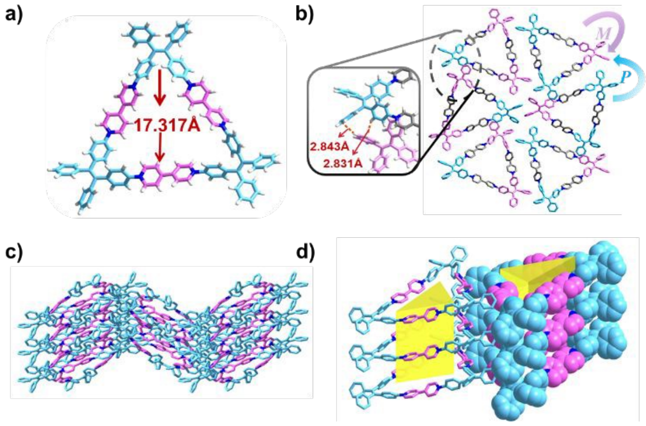

Figure 1 X-ray crystal structures of $\mathbf{T}^{6+}\cdot 6PF_6^-$: (a) and (b) top view, (c) side view of tacking networks from the *c*-axis, (d) side view of a nanochannel formed from nanotubes from the *b*-axis.

Subsequently, radical $\mathbf{T}^{3(+\bullet)}$ was further reduced to the neutral **T** by adding sodium, and the system color gradually changed to reddish brown. The absorption peaks at 660 nm and 720 nm disappeared from the UV-Vis absorption spectrum, and the radical cation signals in the electron paramagnetic resonance (EPR) spectrum vanished as well (Figure 2e), returning to the pre-reduction state. Notably, $CoCp_2$ was also found to induce the same reduction. Upon adding increasing equivalents of $CoCp_2$ (1.0 eq. to 6.0 eq.) to the DMF solution of $\mathbf{T}^{6+}$, significant changes were observed in the UV-Vis spectrum. The radical absorption peaks gradually increased to their maximum intensity at 3.0 eq. $CoCp_2$, indicating the generation of radical $\mathbf{T}^{3(+\bullet)}$. As the $CoCp_2$ concentration increased from 4.0 eq. to 6.0 eq., the radical absorption peaks began to decrease and eventually disappeared, signalling the further reduction of radical $\mathbf{T}^{3(+\bullet)}$ to the neutral **T** (Figures 2f and S13).

When the radical $\mathbf{T}^{3(+\bullet)}$ was exposed to air without nitrogen protection, UV absorption plots at 660 nm and 720 nm were recorded over time. Exposure to air resulted in gradual oxidation of $\mathbf{T}^{3(+\bullet)}$ to the cationic $\mathbf{T}^{6+}$, demonstrating its good reversible redox properties (Figure 2g). A similar phenomenon was observed when $\mathbf{D}^{2+}$ underwent chemical redox reactions to generate radical $\mathbf{D}^{+\bullet}$ and neutral **D** (Figures S10-S12). Notably, the reversible redox transitions of $\mathbf{T}^{6+}/\mathbf{D}^{2+}$ could be observed not only via chemical reduction but also through electrochemical reduction. To explore their potential in electrochromic applications, we fabricated proof-of-concept electrochromic devices (ECDs) using DMF solutions of $\mathbf{T}^{6+}/\mathbf{D}^{2+}$ as the active materials. The ECDs based on $\mathbf{T}^{6+}/\mathbf{D}^{2+}$ exhibited green and dark

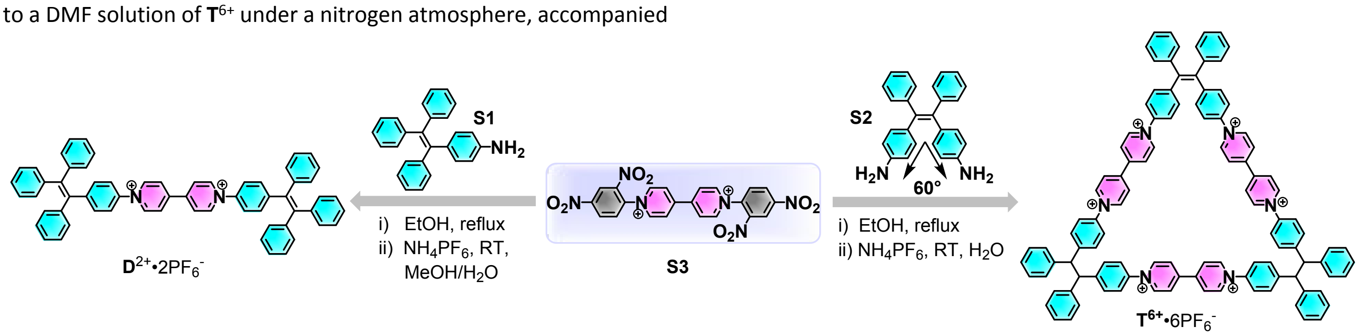

Scheme 1 Synthetic route to $\mathbf{T}^{6+}\cdot 6PF_6^-$ and $\mathbf{D}^{2+}\cdot 2PF_6$.

ChemComm

View Article Online
DOI: 10.1039/D5CC03589A

COMMUNICATION

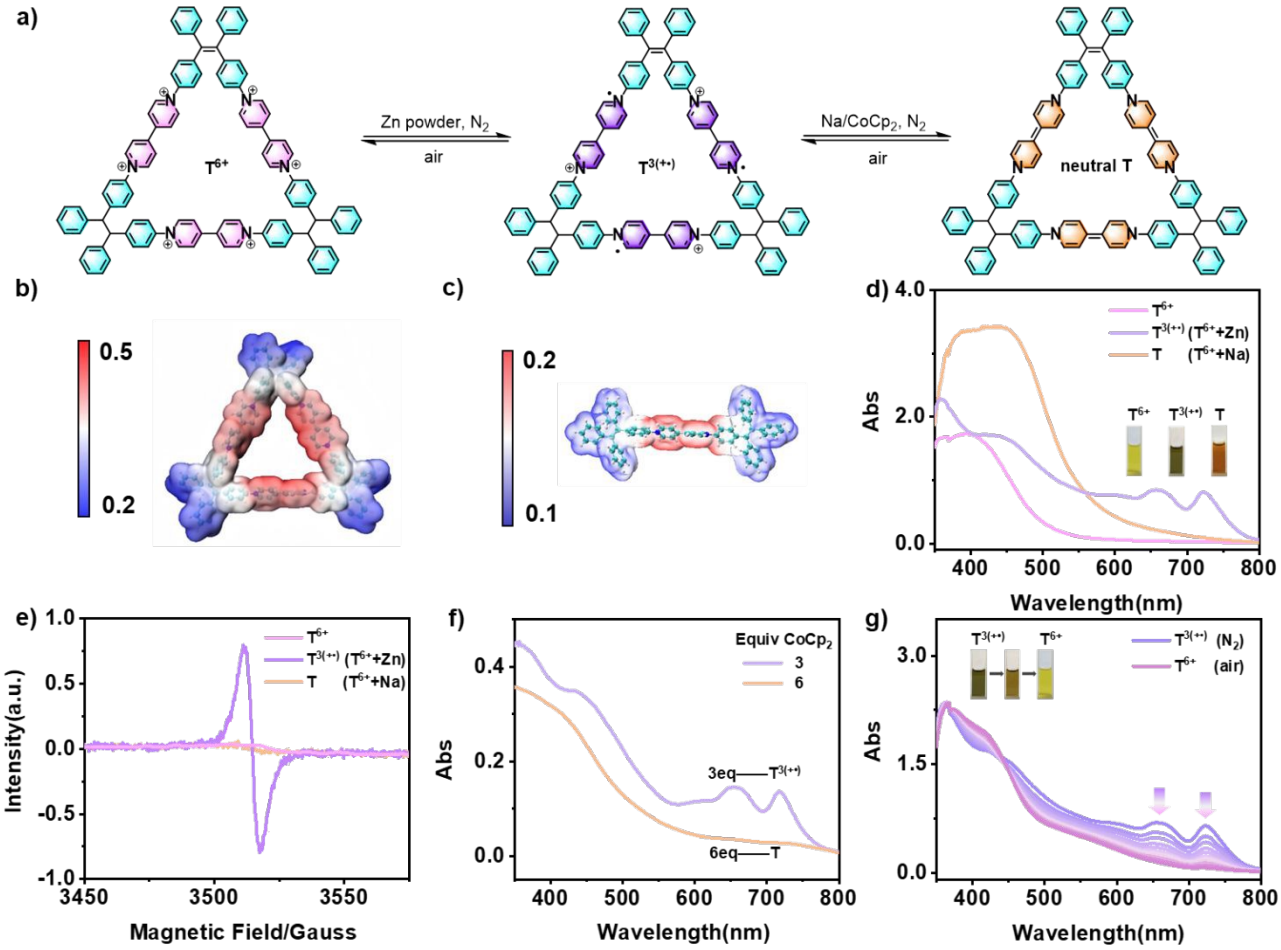

Figure 2 (a) A Schematic representation of the two-step reduction of $\mathbf{T}^{6+}$. Electrostatic potential surfaces of (b) $\mathbf{T}^{6+}$ and (c) $\mathbf{D}^{2+}$. (d) UV/vis spectra of $\mathbf{T}^{6+}$, $\mathbf{T}^{3(+\bullet)}$, and neutral **T** in DMF (c = 10 μM). (e) EPR spectra of the $\mathbf{T}^{6+}$, $\mathbf{T}^{3(+\bullet)}$ and **T**. (f) UV/vis spectra of $\mathbf{T}^{3(+\bullet)}$ generated from chemical reduction of a DMF solution of $\mathbf{T}^{6+}$ upon addition of 1 eq. and 6 eq. of $CoCp_2$ (g) UV/vis spectrum of radical $\mathbf{T}^{3(+\bullet)}$ oxidized in air. The inset photographs of $\mathbf{T}^{6+}$, $\mathbf{T}^{3(+\bullet)}$ and neutral **T** in DMF upon daylight.

green colors when external voltages of 1.5 V and 2.5 V were applied, respectively (Figure 3a and S14a). This color change indicated the accumulation of radicals ($\mathbf{T}^{3(+\bullet)}$/$\mathbf{D}^{+\bullet}$) under voltage application. Upon increasing the voltage further to 2.5 V and 4 V, the radical cations ($\mathbf{T}^{3(+\bullet)}$/$\mathbf{D}^{+\bullet}$) gradually converted to their neutral forms (**T**/**D**), resulting in distinct color transitions from red to red-brown.

Furthermore, the spectroelectrochemistry of ECDs with $\mathbf{T}^{6+}$ as the active material was investigated. The spectroelectrochemical behaviour of $\mathbf{T}^{6+}$ showed two strong absorption peaks at 650 nm and 717 nm (Figure 3b) when a potential of 2.5 V was applied, with a noticeable increase in absorption in the visible region due to the formation of the radical state $\mathbf{T}^{3(+\bullet)}$. As the applied potential was increased to 4 V, $\mathbf{T}^{3(+\bullet)}$ was gradually converted to the neutral **T**, accompanied by a decrease in absorption in the visible region (Figure 3c). A similar two-step reduction process was observed in ECDs based on $\mathbf{D}^{2+}$ when external voltages were applied. Compared to $\mathbf{T}^{6+}$, the ECDs based on $\mathbf{D}^{2+}$ showed a lower reduction voltage (Figures 3d and S14b), indicating that $\mathbf{D}^{2+}$ is more readily reduced (electron-receptive). Notably, compared to $\mathbf{D}^{2+}$-based ECDs (Figure S14b-c), the $\mathbf{T}^{6+}$-based ECDs demonstrated three times higher radical stability after 40 seconds of voltage cutoff. As a result, the color of $\mathbf{T}^{6+}$-based ECDs remained stable for a longer period after the power supply was disconnected (Figure 3e), indicating greater radical stability and fewer cycles required for regeneration.

In summary, a hexacationic triangular macrocycle $\mathbf{T}^{6+}\cdot 6PF_6^-$, composed of TPE derivative as apexes, was successfully created in a one-pot manner via Zincke reaction. In the crystalline state, conformational *PPM*-$\mathbf{T}^{6+}$ and *MMP*-$\mathbf{T}^{6+}$ isomers formed 3D nanotubular framework via multiple C-H...π interactions. Moreover, $\mathbf{T}^{6+}\cdot 6PF_6^-$ exhibited AIE property under the regulation of solvent effect. Notably, $\mathbf{T}^{6+}\cdot 6PF_6^-$ underwent three reversible redox states via chemical reduction and electrochemical reduction, displaying good redox properties, and along the cyclization of $\mathbf{T}^{6+}\cdot 6PF_6^-$, two-step reduction potentials became distinctly negative with

increasing LUMO energy levels. These above-mentioned results guided us to build an electrochromic component by utilizing **T**$^{6+}$·6PF$_6^-$, we found that the color of the system gradually deepens as the applied voltage increases, and the radical stability is three times higher than that before cyclization. This work enlightens us to construct shape-persistent macrocycles via angle-controllable synthesis strategies, which further provides a theoretical basis for the chemical reduction and electrochromism of macrocycles.

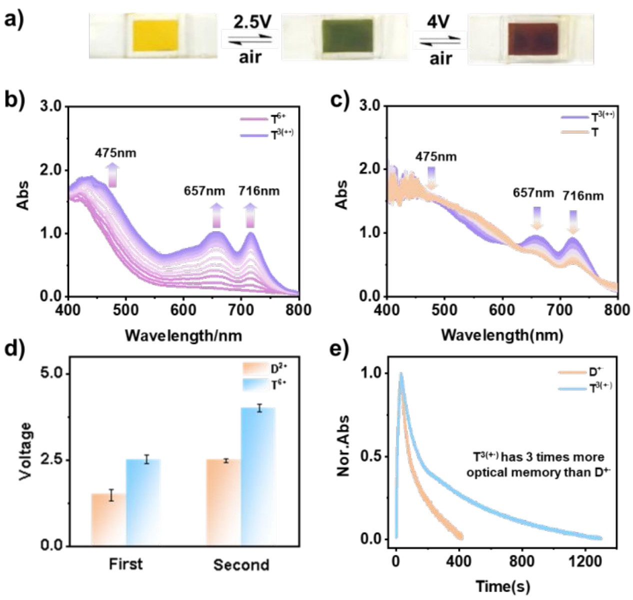

Figure 3 (a) A solution-based ECDs with **T**$^{6+}$ as an electrochromic material. Spectroelectrochemistry of **T**$^{6+}$ ($c = 1 \times 10^{-3}$ M) for (b) the first reduction and (c) the second reduction. (d) Two reduction voltage values of **T**$^{6+}$/**D**$^{2+}$. (e) The optical memory of **T**$^{3(+•)}$/**D**$^{+•}$.

This work was supported by the National Natural Science Foundation of China (Nos. 22301241 and 22371229), and the Shaanxi Fundamental Science Research Project for Chemistry and Biology (22JHQ073).

Conflicts of interest

There are no conflicts to declare.

Data availability

All synthetic procedures, compound characterization data is available in the supporting information. Crystallographic data have been deposited in the Cambridge Crystallographic Data Centre (CCDC 2364408).

Notes and references

1. Y. Chen, C. Qian, Q. Zhao, M. Cheng, X. Dong, Y. Zhao, J. Jiang, L. Wang. *Chem. Commun.,* 2019, **55**, 8072-8075.
2. G.-B. Huang, S.-H. Wang, H. Ke, L.-P. Yang, W. Jiang. *J. Am. Chem. Soc.*, 2016, **138**, 14550-14553.
3. T. Ogoshi, S. Kanai, S. Fujinami, T.-A. Yamagishi, Y. Nakamoto. *J. Am. Chem. Soc.*, 2008, **130**, 5022-5023.
4. I. Roy, S. Bobbala, R. M. Young, Y. Beldjoudi, M. T. Nguyen,M. M. Cetin, J. A. Cooper, S. Allen, O. Anamimoghadam, E. A. Scott, M. R. Wasielewski, J. F. Stoddart. *J. Am. Chem. Soc.*, 2019, **141**, 12296-12304.
5. Q. Shi, C.-F. Chen. *Org. Lett.,* 2017, **19**, 3175-3178.
6. Y. Han, Z. Meng, Y.-X. Ma, C.-F. Chen. *Acc. Chem. Res.,* 2014, **47**, 2026-2040.
7. T. Ogoshi, T.-A. Yamagishi, Y. Nakamoto. *Chem. Rev.,* 2016, **116**, 7937-8002.
8. G. Yu, K. Jie, F. Huang. *Chem. Rev.,* 2015, **115**, 7240-7303.
9. R. Chakrabarty, P. S. Mukherjee, P. J. Stang. *Chem. Rev.,* 2011, **111**, 6810-6918.
10. P. J. Stang, B. Olenyuk. *Acc. Chem. Res.,* 1997, **30**, 502-518.
11. X. Yan, S. Li, T. R. Cook, X. Ji, Y. Yao, J. B. Pollock, Y. Shi, G. Yu, J. Li, F. Huang, P. J. Stang. *J. Am. Chem. Soc.*, 2013, **135**, 14036-14039.
12. B. Jiang, L.-J. Chen, Y. Zhang, H.-W. Tan, L. Xu, H.-B. Yang. *Chin. Chem. Lett.*, 2016, **27**, 607-612.
13. X. Yan, J.-F. Xu, T. R. Cook, F. Huang, Q.-Z. Yang, C.-H. Tung, P. J. Stang. *Proc. Natl. Acad. Sci.*, 2014, **111**, 8717-8722.
14. Z.-Y. Li, Y. Zhang, C.-W. Zhang, L.-J. Chen, C. Wang, H. Tan, Y. Yu, X. Li, H.-B. Yang. *J. Am. Chem. Soc.,* 2014, **136**, 8577-8589.
15. B. Sun, M. Wang, Z. Lou, M. Huang, C. Xu, X. Li, L.-J. Chen, Y. Yu, G. L. Davis, B. Xu, H.-B. Yang, X. Li. *J. Am. Chem. Soc.*, 2015, **137**, 1556-1564.
16. M. Mastalerz. *Acc. Chem. Res.*, 2018, **51**, 2411-2422.
17. R. D. Mukhopadhyay, Y. Kim, J. Koo, K. Kim. *Acc. Chem. Res.*, 2018, **51**, 2730-2738.
18. M.-X. Wang. *Acc. Chem. Res.*, 2012, **45**, 182-195.
19. X.-Y. Lou, Y.-W. Yang. *Aggregate*, 2020, **1**, 19-30.
20. M. T. Nguyen, M. D. Krzyaniak, M. Owczarek, D. P. Ferris, M. R. Wasielewski, F. J. Stoddart. *Angew. Chem. Int. Ed.,* 2017, **56**, 5795-5800.
21. T. Zincke, G. Weißpfenning. Über *Justus Liebigs Ann. Chem*., 1913, *396*, 103.
22. T. Zincke, W. Würker. Ueber *Justus Liebigs Ann. Chem*., 1905, **341**, 365.
23. L. Tong, D. Zhu, B. Chen, Y. Chen, G. Wu, F. Zeng, H. Li. *Org. Lett.,* 2021, **23**, 9343-9347.
24. H. M. Colquhoun, B. W. Greenland, Z. Zhu, J. S. Shaw, C. J. Cardin, S. Burattini, J. M. Elliott, S. Basu, T. B. Gasa, J. F. Stoddart. *Org. Lett*., 2009, **11**, 5238.
25. M. Kathiresan, B. Ambrose, N. Angulakshmi, D. E. Mathew, D. Sujatha, A. M. Stephan. *J. Mater. Chem. A*, 2021, **9**, 27215-27233.
26. Y. Li, N. Li, G. Li, Y. Qiao, M. Zhang, L. Zhang, Q.-H. Guo, G. He. *J. Am. Chem. Soc*., 2023, **145**, 9118-9128.
27. Z. Bai, X. Wu, R. Fang, Z. Lu, C. Hou, Q. Zhang, Y. Li, K. Li, H. Wang. *Adv. Funct. Mater*., 2024, **34**, 2312587.
28. X. Wu, Q. Fan, Z. Bai, Q. Zhang, W. Jiang, Y. Li, C. Hou, K. Li, H. Wang. *Small,* 2023, **19**, 2301742.
29. Q. Zhang, R. Toyoda, L. Pfeifer, B. L. Feringa. *J. Am. Chem. Soc.,* 2023, **145**, 6976-6985.
30. L. He, Y. Jiang, J. Wei, Z. Zhang, T. Hong, Z. Ren, J. Huang, F. Huang, P. J. Stang, S. Li. *Nat. Comm.,* 2024, **15**, 3050.
31. (a) J. Li, R. Li, J. Liu, J.-Q. Liu, J. Xu, X. Zhou, Y. Zhang, K. Wang, L. Lei, G. Xie, F. Wang, Y. Yang, L. Cao. *Chin. Chem. Lett*., 2024, **35**, 110355. (b) D. Chang, X. Xiao, D. An, R. Zhang, X. Song, Y. Liu, Y. Zhao, X. Lu, *Aggregate*, 2023, **4**, e380.
32. X.-N. Sun, A. Liu, K. Xu, Z. Zheng, K. Xu, M. Dong, B. Ding, J. Li, Z.-Y. Zhang, C. Li. *Aggregate*, 2024, **5**, e607.
33. H.-S. Xu, Y. Luo, R. Li, W.-N. Jiao, S. Huang, W.-D. Zhu, H. Wang, T. Chen, M. Nero, F. Chen, Q. Gao, X. Li, M. Pan, T. Willhammar, K. P. Loh, C.-Y. Su. *Nat. Synth.*, 2024, **3**, 1498-1506.
34. Y. Yu, Y. W. Li, X. Q. Wang, H. Nian, L. Wang, J. Li, Y. X. Zhao, X. R. Yang, S. M. Liu, L. Cao, J. Org. Chem. 2017, 82, 5590-5596.

View Article Online
DOI: 10.1039/D5CC03589A

Data Availability Statement

All synthetic procedures, compound characterization data is available in the supporting information. Crystallographic data have been deposited in the Cambridge Crystallographic Data Centre (CCDC 2364408).